1

# Graphene confers ultra-low friction on nanogear cogs

3

Andrea Mescola[1#], Guido Paolicelli[1#], Sean P. Ogilvie[2$], Roberto Guarino[3$], James G. McHugh[4],

Alberto Rota[1,5], Erica Iacob[6], Enrico Gnecco[7], Sergio Valeri[1,5], Nicola M. Pugno[8, 9], Venkataramana

Gadhamshetty[10], Maksud M. Rahman[11], Pulickel Ajayan[11*], Alan B. Dalton[2*], Manoj Tripathi[2*]

7

[1] CNR-Istituto Nanoscienze - Centro S3, Via Campi 213 41125 Modena, Italy

[2] Department of Physics and Astronomy, University of Sussex, Brighton BN1 9RH, U.K.

[3] École Polytechnique Fédérale de Lausanne (EPFL), Swiss Plasma Center (SPC), CH-5232

Villigen PSI, Switzerland

[4] Department of Chemistry, Loughborough University, Loughborough LE11 3TU, United Kingdom

[5] Department of Physics, Informatics and Mathematics, University of Modena and Reggio Emilia,

Via Campi 213 41125 Modena, Italy

[6] Fondazione Bruno Kessler, Sensors and Devices, via Sommarive 18, 38123 Trento, Italy

[7] Otto Schott Institute of Materials Research, Friedrich Schiller University Jena, D-07743 Jena,

Germany

[8] Laboratory of Bio-Inspired, Bionic, Nano, Meta, Materials & Mechanics, Department of Civil,

Environmental and Mechanical Engineering, University of Trento, Via Mesiano, 77, 38123 Trento,

Italy

[9] School of Engineering and Materials Science, Queen Mary University of London, Mile End Road,

London E1 4NS, UK

[10] Department Civil and Environmental Engineering, South Dakota School of Mines and

Technology, Rapid City, South Dakota 57701, USA

[11] Department of Materials Science and Nanoengineering, Rice University, Houston, TX 7705, USA

26

*Corresponding authors

# First author contributed equally

$ Authors contributed equally

30

**Abstract:** Friction-induced energy dissipation impedes the performance of nanomechanical devices. Nevertheless, the application of graphene is known to modulate frictional dissipation by inducing local strain. This work reports on the nanomechanics of graphene conformed on different textured silicon surfaces that mimic the cogs of a nanoscale gear. The variation in the pitch lengths regulates the strain induced in capped graphene revealed by scanning probe techniques, Raman spectroscopy and molecular dynamics simulation. The atomistic visualisation elucidates asymmetric straining of C-C bonds over the corrugated architecture resulting in distinct friction dissipation with respect to the groove axis. For the first time, we reported experimental results for strain-dependent solid lubrication which can be regulated by the corrugation and leads to ultra-low frictional forces. Our results are applicable for graphene covered corrugated structures with movable components such as nanoelectromechanical systems, nanoscale gears, and robotics.

**Introduction**

Engineering nanostructure through laser texturing, ion milling and photolithography has significantly improved the sensing performance of nano and microelectromechanical systems (NEMS and MEMS)[1,2] devices by tuning wetting characteristics[3], nano-channeling[4], optical[5], mechanical[6] and electronic properties[7]. The requirement for nano/micro-machines has surged recently, with focus progressing towards miniaturized devices[7,8]. In the field of tribology, textured surfaces with micro or nanoscale dimples, grooves, pillars and other geometries are found to be beneficial for optimized adhesion and friction forces[9]. Unlike macroscale textured surfaces[10,11], the nano-scaled structured geometry pose tremendous challenges for performance and efficiency when they are in physical contact with one another (e.g. gear operation at the nanoscale)[8]. Interaction forces that are relatively weak at the macro-scale (such as van der Waals and capillary forces) become dominant at the nanoscale. Therefore, nanostructured devices are often susceptible to conditions of extreme pressure, friction, and adhesion[12]. The nanoscale contacts exert enormous pressure at the interface even at low values of the applied normal force, subsequently leading to friction-induced wear[13]. Thus, a novel strategy is needed to regulate these forces at the nanoscale.

Several approaches have been adapted to tune the friction force by introducing liquid-state lubricants such as organic oils[10,14], ionic liquids[15,16], and tribological buffer layers such as polymer brushes[17]. Nevertheless, the ecologically harmful effect of liquid-state lubricants[18] and their inefficiency in

confined conditions related to viscosity modifications hinder their tribological performance[14]. A potential alternative is presented by using solid-state lubricants[19], in the form of nanoparticles or lamellar solids such as graphite, transition metal dichalcogenide (TMD) e.g. molybdenum disulfide)[20,21] and recently reported the emerging class of MXenes (2D transition metal carbides, nitrides, and carbonitrides)[22]. TMDs and MXenes have demonstrated impressive mechanical performance and potential for possible tribological applications[23,24,25]. One of the most promising solutions to protect surfaces at the nanoscale level relies on epitaxially grown graphene and its residue-free transfer technique[26]. Graphene has the lowest bending rigidity[27,28] coupled to high in-plane intrinsic strength[29] and is inert in humid and corrosive atmospheres[30]. However, the substrate on which graphene is deposited plays a pivotal role in modulating the mechanical, physical and electronic properties of the graphene film[31,32]. In particular, strain induced by interaction with a substrate is one of the most intriguing parameters to adapt and tune graphene characteristics[33,34]. The role of substrate shape and its interfacial adhesion with graphene is theoretically studied by Wagner *et al.* [35] and observed the "snap-through" event of graphene under different textured confinements. They presented the transformation of graphene membrane from flat to conforming states relate to its bending rigidity which is useful to regulate the strain. The induced strain or strain gradient fields[36–38] has a correlation with tribological characteristics of graphene and other 2D materials ($MoS_2$) for strain-induced lubrication[21]. In another approach, modulation of frictional characteristics in graphene through functionalization (such as fluorination) is reported and hypothesized the role of flexural stiffness attributed to the higher frequency of flexural phonons for enhancing frictional signals[39,40]. Nevertheless, the results are limited in the consideration of any elastic system and adhesion force towards the tip apex. In the absence of functionalization, the increase in bending stiffness in 2D material with adding atomic layer causes decreases in friction dissipation, as thicker graphene is lesser susceptible to deform out-of-plane and ceased to adhere with tip[41]. Similarly, our previous work[42] demonstrated lowering of friction force for covalently bonded interface for Gr/Ni (111) than weak van der Waals (vdW) Gr/Silica interface due to lesser availability of graphene towards tip apex. Recently, the contact quality between suspended graphene and tip apex is altered through symmetrical in-plane straining in graphene by depositing over circular-shaped textured structure in pressurized conditions to achieve a super lubricating state[43]. Nevertheless, the frictional response of asymmetric strained graphene over the textured surface is a rarely addressed topic, which may play a crucial role in the durability of NEMS devices. Nevertheless, the frictional response of asymmetric strained graphene over the textured surface is a rarely addressed topic, which may play a crucial role in the durability of NEMS devices.

96    In the present study, we investigate the interplay between texture-induced strained graphene and its

97    ability to lubricate. To do this, we employ nano-textured silicon surfaces as substrates that mimic the

98    cogs of a nanogear and use friction force microscopy (FFM) measurements in ambient conditions to

99    elucidate the effect of graphene deposition on the local friction properties. The different aspect ratios

100   (depth/pitch) of the grooves modulate the conformation/suspension of graphene, resulting in it being

101   strained. Raman spectroscopy shows the substrate-induced compressive strain in graphene over a flat

102   surface, which systematically released as pitch length decreases. Molecular dynamics simulations

103   corroborate the Raman measurements and elucidate the atomic-scale resolution of graphene

104   corrugation. Simulation results identify an asymmetric strain distribution through lattice expansion

105   and contraction of the C-C bond at different orientations. This work demonstrates, for the first time,

106   the regulation of the frictional dissipation in nanoscale architecture through strain engineering of

107   graphene.

108   **Results and discussion**

109   Atomic force microscopy (AFM) images in **Figure 1(a, b, c)** show the typical morphology of

110   graphene-covered textured surfaces referred to as GrP40, GrP125 and GrP250. The preparation and

111   characterisation of the textured surface is described in previous work[44,45] and in Supplementary

112   Information **S1**. Each textured region comprises long parallel grooves approximately 40 nm wide; the

113   grooves' spacing referred to pitch length (P) varies from $40 \pm 4$, $125 \pm 8$ and $250 \pm 14$ nm. A chemical

114   vapour deposition-grown single layer of graphene has been deposited over the textured surfaces by

115   the wet transfer method[46]. The topographic profiles of bare and covered surfaces, presented in **Figure**

116   **1 (d, e, and f),** illustrate the physical corrugation of graphene on the substrate. The measured depth

117   of the grooves is between 2.4-3nm on bare P40 and is reduced by 10-15% after graphene deposition

118   measured from bottom of trough. On the other hand, groove depths of bare P125 and P250 are ~ 4nm

119   and are reduced by 7-10% in GrP125 and 3-5% GrP250, respectively, revealing higher conformation

120   depth of graphene at GrP250. For GrP40 corrugation, suspension of graphene does not reach the stage

121   of complete "snap-through"; and, a partial conformal contact is achieved[35]. Thus, graphene can be

122   considered as a membrane clamped between two grooves that induce different strains (see

123   Supplementary **Figure S1**).
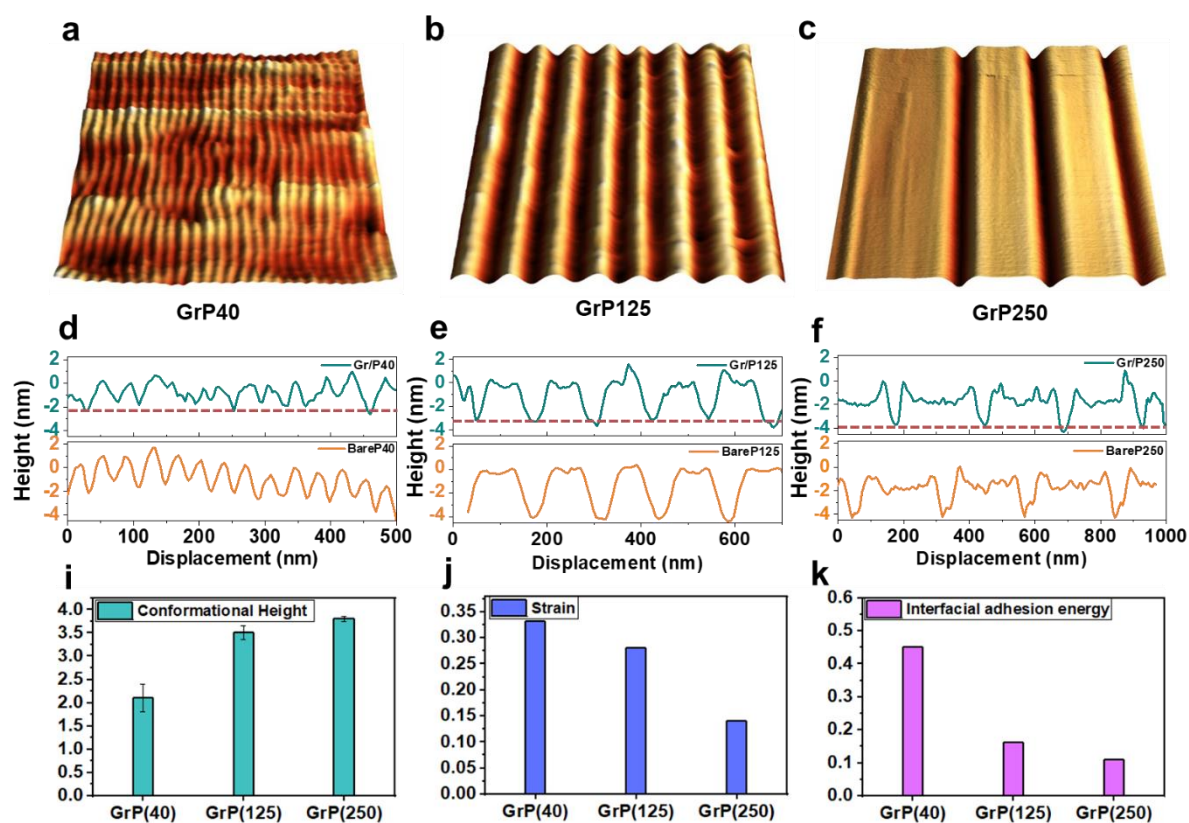
**Figure1: Morphology of graphene covered textured surfaces.** AFM topography of graphene covered textured surface of pitch (a) $40 \pm 4$ nm, (b) $125 \pm 5$ nm and (c) $250 \pm 8$ nm. (d)-(f) Topographical line profiles of bare and graphene covered textured surfaces across the grooves for covered (dark cyan) and bare surface (orange) colour. The interfacial interaction between graphene and textured surfaces of different pitch lengths through (i) conformational height, (j) strain (%) and (k) interfacial adhesion energy.

The conformation of graphene over the patterned surface unravel the mechanics of graphene as an act of balancing between interfacial adhesion and elastic energy stored in the graphene sheet(i.e., bending and stretching)[47,48]. The conformation induced average transverse strain ($\varepsilon$) and interfacial adhesion energy (meVÅ$^{-2}$) between graphene and textured surfaces, calculated from the height profiles, are reported in **Figure 1(i, j, k)** (see Supplementary Information **S2** for details). The systematic variations in the strain values indicating the contribution from the textured surfaces for their tendency to reduce compressive strain which is induced at the flat surface. The observation that the interaction (interfacial adhesion energy) between graphene and P40 is higher derives directly from the need of compensating a larger stretching energy (due to a corresponding larger compressive strain).

The substrate-induced stretching/compression of single-layer graphene and the doping for each textured surface have been quantified by comparing Raman spectroscopy on the flat region (Gr/Flat)

143    and graphene-covered textured surfaces (GrP40 to GrP250). The Raman modes of G peak position

144    (PosG) and 2D peak position (Pos2D) are associated with strain, since a change in lattice constant

145    leads to a variation in the phonon modes. Furthermore, these modes are useful for detecting carrier

146    concentration (n) due to alteration in bond length and non-adiabatic electron-phonon coupling[50]. The

147    relation between strain and doping of graphene with PosG and Pos2D is described in Supplementary

148    Information **S3.** It is well recognised that physically deposited graphene on a flat Si substrate results

149    in a p-type doped system under compressive strain[51]. The textured regions reduce the compressive

150    strain in graphene with smaller P values. This phenomenon is observed through gradual phonon

151    softening of G and 2D Raman modes of graphene deposited over Gr/Flat, GrP250, GrP125 and

152    GrP40; see **Figure 2a, b**. Nevertheless, we did not observe the splitting of either G and 2D modes,

153    which indicates that the magnitude of the induced strain is not appreciably high ($<0.35\%$)[52].

154    The correlation plot in **Figure 2c** shows the distribution of Pos2D as a function of PosG with the

155    mean value of the distribution represented by stars. The strain axis and doping axis are drawn at the

156    slope ($\partial$Pos2D/$\partial$PosG) range 2.25-2.8 and 0.75, respectively[53,54]. The intersection of both axes is

157    assumed to be a point of minimal strain and doping in suspended graphene with the coordinates taken

158    from the work of Lee *et al.*[54].Thus, the distribution of all Raman data deviated from the intersection

159    coordinates is used to predict strain and doping values. The correlation plot illustrates a relative

160    change in the average compressive strain ($\varepsilon$) for Gr/flat of $\approx$- 0.09%, which is transformed on

161    corrugated surfaces as follows: P= 250 nm ($\varepsilon \approx$- 0.07%), P = 125 nm ($\varepsilon =$- 0.061%), P = 40 nm ($\varepsilon =$

162    0.02%). This validates the argument of releasing compressive strain in graphene in the textured

163    regions relative to the flat surface. It is worth noting that the Raman laser spot diameter using a 100X

164    (objective lens) is approximately 700 nm. Therefore, the measured strain and the carrier concentration

165    values are averaged over several crests, troughs, and flat regions in each spectrum. Nevertheless, the

166    distinct clusters of points in the correlation plots indicate the well-defined modulation of Raman

167    modes, and its associated strain and doping dictated by the substrate corrugation, Supplementary

168    **Figure S2**. One can get a higher spatial resolution up to 25- 40 nm and enhanced Raman scattering

169    signals through tip-enhanced Raman spectroscopy (TERS) for monitoring the contribution from the

170    individual groove of the graphene covered textured surface [55]. This technique would be useful to

171    investigate the change in the graphene lattice over the grooves and its associated electronic structure

172    to be considered in near future.

173    Unlike flat or multi-axial strained surfaces (e.g. suspended graphene over a circular trench),

174    corrugated surfaces can induce anisotropy in strained graphene owing to the asymmetric stretching

175    of carbon atoms oriented along parallel and perpendicular directions relative to the groove axis as

found by Lee and coworkers[56]. The atomic-scale features of the graphene conformation over the textured silicon surfaces have been investigated using molecular dynamics (MD) and density functional theory (DFT) calculations of the graphene/Si at different pitch lengths, see supplementary **S4** for DFT and MD set-up. The crest region of GrP250 shows higher compressive strain induced through contact with the Si substrate, while the neighbouring trough exhibits curvature-induced tensile strain, which decreases with pitch length down to GrP40. The magnitude of the net compression over a crest is proportional to the area of the graphene in direct contact with the Si substrate, and is therefore higher than the tension across the trough. This leads to a decreasing average value of compression, as shown in **Figure 2(d)**, which is in excellent agreement with our Raman spectroscopic measurements. A similar trend was observed by Zhang *et al.*[49] on biaxially strained graphene covered self-assembled texturized silicon nanospheres with different diameters. In that arrangement, the authors reported a transformation of compressive strain into tensile strain in graphene deposited over smaller spherical particles due to the increasing real contact area at the apex. Hinnefeld *et al.*[53] found a similar trend for graphene suspended on silicon pillars with a separation distance of 600 nm indicating an increase in charge carrier concentration and decreased compressive strain. Here, by reducing the textured spacing by one order of magnitude (i.e. $\approx 40$ nm), we find that the deposited graphene potrays characteristics of both strain and doping of a partially suspended sheet. The net height variation is illustrated in the inset **Figure 2(d,** see scale bar**)**. Notably, there is a generation of ripples in the suspended region due to the release of the  net compressive strain. This phenomenon was further analyzed by FFM.
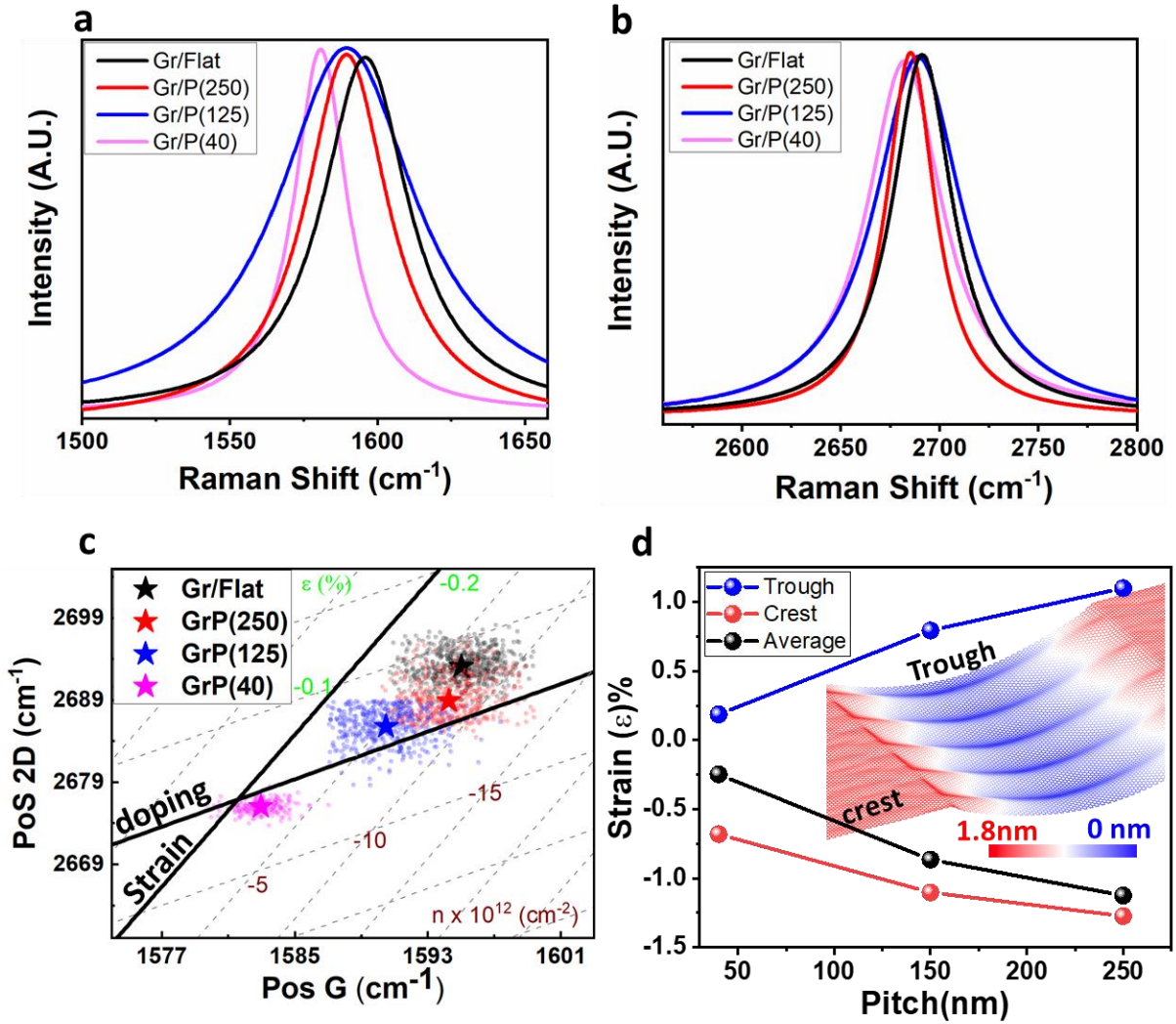
**Figure2: Raman spectrum of graphene covered textured region.** Raman spectrum of (a) PosG (cm$^{-1}$) and (b) Pos2D (cm$^{-1}$) for graphene covered flat surface and different textured regions. (c) Correlation plot of PosG vs Pos2D phonon modes for deconvoluted strain and doping in graphene from flat to the textured regions. The data distribution is from 50-70 Raman spectra and the mean values are represented by star-shaped points. The strain ($\varepsilon$) and doping (n) axis classify the distribution of Raman data. (d) The bond strain distribution at the crest, trough and averaged over the entire surface (black colour data) for different pitch lengths measured from MD simulations. Inset shows the net height (Z-scale) variation at crest and trough regions for GrP40 under the influence of net tensile and compressive strain.

As Raman analysis suggests that the Gr/Flat and GrP(40) configurations provide the most pronounced differences in strain values, these extreme surfaces were chosen for FFM[57] measurements. Due to the intrinsic anisotropy in the texture-induced strain in graphene, FFM measurements were performed in orthogonal **(Figure 3a-c)** and parallel **(Figure 3d-f)** directions relative to the groove axis of GrP(40)

(details about procedure and calibration are reported in Supplementary Information **S5**). The FFM images on the GrP40 sample comprises bare textured silicon regions and nearby graphene covered areas in a single acquisition. In this way, bare and covered textured surfaces are compared under similar contact conditions, so that the local environment and possible geometrical effects or tip shape contributions can be disentangled (see **Figure S5** for estimation of tip curvature radius). There is a significant contrast in the lateral force values between bare and covered graphene for both orientations (**Figure 3b, e**), which evidences the excellent lubrication performance of single-layer graphene over the periodic surface. The presence of graphene reduces the average friction force up to 10 times compared to the bare surface under similar applied load conditions ranging from 10-30 nN, with no edge failure noticeable. These results are in agreement with previous nanotribological characterizations of graphene on flat silicon substrates[58–60] and lower than crystal and polycrystalline CVD $MoS_2$[25] and comparable to hBN/silica[61]. The lateral force profile in **Figure 3c** shows a markedly distinguishable undulated friction force response between graphene-covered and bare silicon, orthogonal to the groove axis. Here, the lateral force is significant with stochastic variation over the bare silicon but is reduced and periodically modulated in the graphene capped region.

While scanning parallel to the groove axis at the capped region, friction force modulation as a function of tip displacement is almost zero, though stochastic lateral force is sustained at the bare surface. This is clearly illustrated in the lateral force map in **Figure 3e** and in the profile drawn orthogonal to the groove axis (**Figure 3f**) to provide a valid comparison with **Figure 3c**. The detailed analysis between crest and trough for the scanned orthogonal and parallel reveals a remarkable difference $(Gr/LF_{Trough\ parallel} - Gr/LF_{crest\ parallel}) \approx 0.2nN$ and $(Gr/LF_{Trough\ orthogonal} - Gr/LF_{crest\ orthogonal}) \approx 1.5nN$; a more than seven-fold increase. The ratio of the friction force at trough/crest measured during the scan in parallel and orthogonal directions at fixed load conditions is $\approx 2$ and $5$, respectively. Thus, the trough region of an orthogonally-scanned textured surface contributes to the highest lateral force, but this effect is suppressed along the parallel-scanned region. On the other hand, the frictional response over the bare Si textured surface scanned in orthogonal and parallel directions is isotropic, as expected for this design of texturing[62]. This indicates that the anisotropic strain distribution in the graphene monolayer plays a pivotal role in regulating the friction force induced from the textured surface.

The texture induced straining in graphene, undulating friction dissipation and anisotropic sliding resistance over the groove axis could be useful in regulating the motion of nanoscale objects, in engineering designer diffusion gradients for adsorbed molecules or even as a smart substrate to effect the proliferation of biological cells for tissue engineering applications. Such a high degree of friction force regulation is not possible over flat surfaces coated in graphene, which shows similar friction

force (isotropic) in different scanning directions, see Supplementary Information (**Figure S6**). While, frictional anisotropy is also reported through different arrangements of carbon atoms in graphene[63,64], here we demonstrate friction force regulation through the graphene-covered textured substrate as a versatile post-treatment for surfaces in nanomechanical devices.
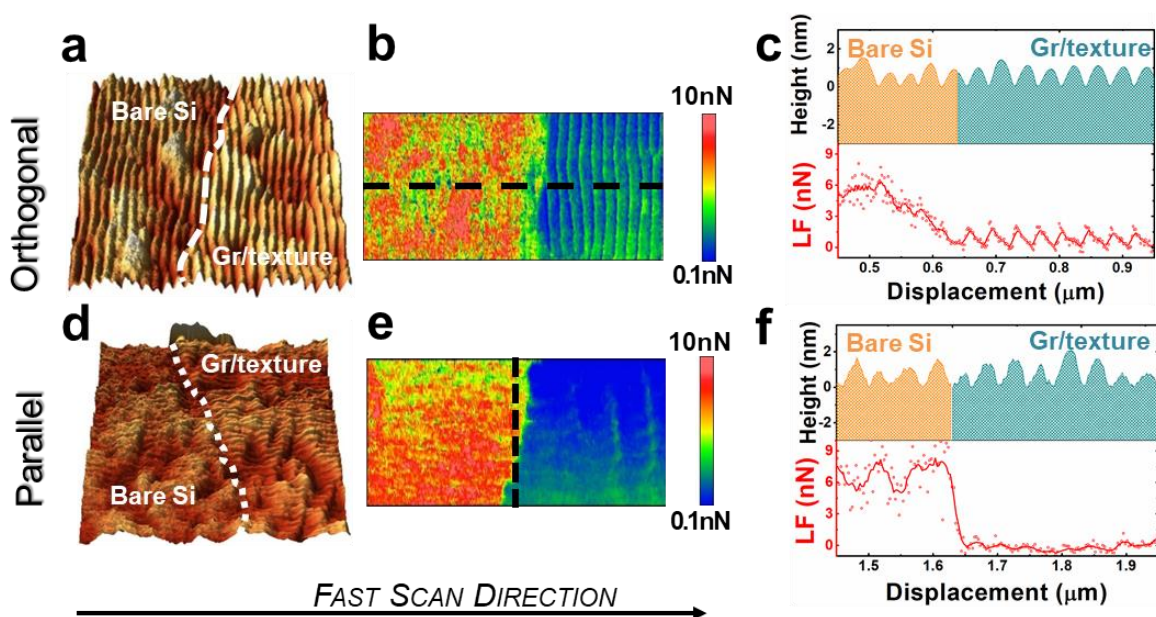


**Figure 3. Effect of scan direction on friction force for GrP(40).** First row shows (a) topography image (1.0 x 1.0 micron) and (b) lateral force map (1.0 x 0.3 micron) measured at applied normal load ≈30nN on GrP40 for grooves axis aligned orthogonal to the fast scan direction. The white dashed line in topography profiles represents the interface between the bare and graphene covered region. (c) Top, height profile (orange colour corresponds to bare silicon, dark cyan colour to graphene covered region) and, bottom, corresponding lateral force profile extracted from black dashed line in (b). Second-row shows (d) topography image (1.0 x 1.0 micron) and (e) lateral force map (1.0 x 0.3 micron) measured on GrP40 for groove axis aligned parallel to the fast scan direction at applied normal load ≈ 25nN. (f) Top, height profile and bottom, corresponding lateral force profile extracted from black dashed line in (e).

The load dependence friction curves for P(40) and GrP(40) are reported in **Figure 4** for orthogonal- and parallel-scanned directions (see details in Supplementary Information **S6**, **Figure S7-S9**). The friction force values for the bare textured region are increased by a factor of 10 as compared to graphene-covered regions for all applied loads range (-10 to 30 nN), consistent with the lateral force

profile. The shear strength (S = friction force/area) of the interface is measured by fitting the data through the Derjaguin-Muller-Toporov (DMT) model (continuous line in **Figure 4 (a, b)**) following 2/3 power law within continuum mechanical modelling of the contact region[65–67] and the coefficient of friction (COF) is measured by a linear fit of the curves (dashed lines). The use of DMT approximation is justified due to low adhesion force at the interfacial contact. Nevertheless, these contact conditions could alter depending on the magnitude of local adhesion force, where different contact conditions (e.g. Johnson-Kendall-Roberts (JKR)) can be implemented as reported by Deng et al.[59] and Lang and coworkers[68].The results are shown in **Figure 5,** revealing a factor of three change in the S(MPa) for GrP40 between parallel and orthogonal directions to the groove axis (38/12 ≈ 3.16). In contrast, S measured for bare P40 for scanned parallel and orthogonal directions found comparable (345/322 ≈ 1.07). Also, S measured for sliding parallel to the groove on GrP40 (S≈ 12 MPa) is lower by ≈ 50% than Gr/Flat (for S≈ 25 MPa),  which is in good agreement with the literature [59,69].

The COF values are corroborated with S revealing minimal values of 0.009±0.001 and 0.011±0.002 at different locations respectively. The COF values for the Gr/Flat surface was found to be intermediate between the orthogonal and parallel scanned axis. Our results are in good agreement with the investigation presented by Zhang and coworkers[43] on tuning the COF by regulating strain in the suspended graphene. The reported COF of the suspended graphene (a region of low strain) is almost double compared to that of strained (0.3%) graphene. The presented textured surfaces demonstrate that crests and troughs serve as distinct strained regions that can regulate the friction force. The FFM values for Gr/Flat represent a compressive strain system, as demonstrated in the Raman correlation plot. Here, sliding of tip under finite normal force leads to elastic buckle formation as a "puckering" effect which leads to the higher friction force values[41].
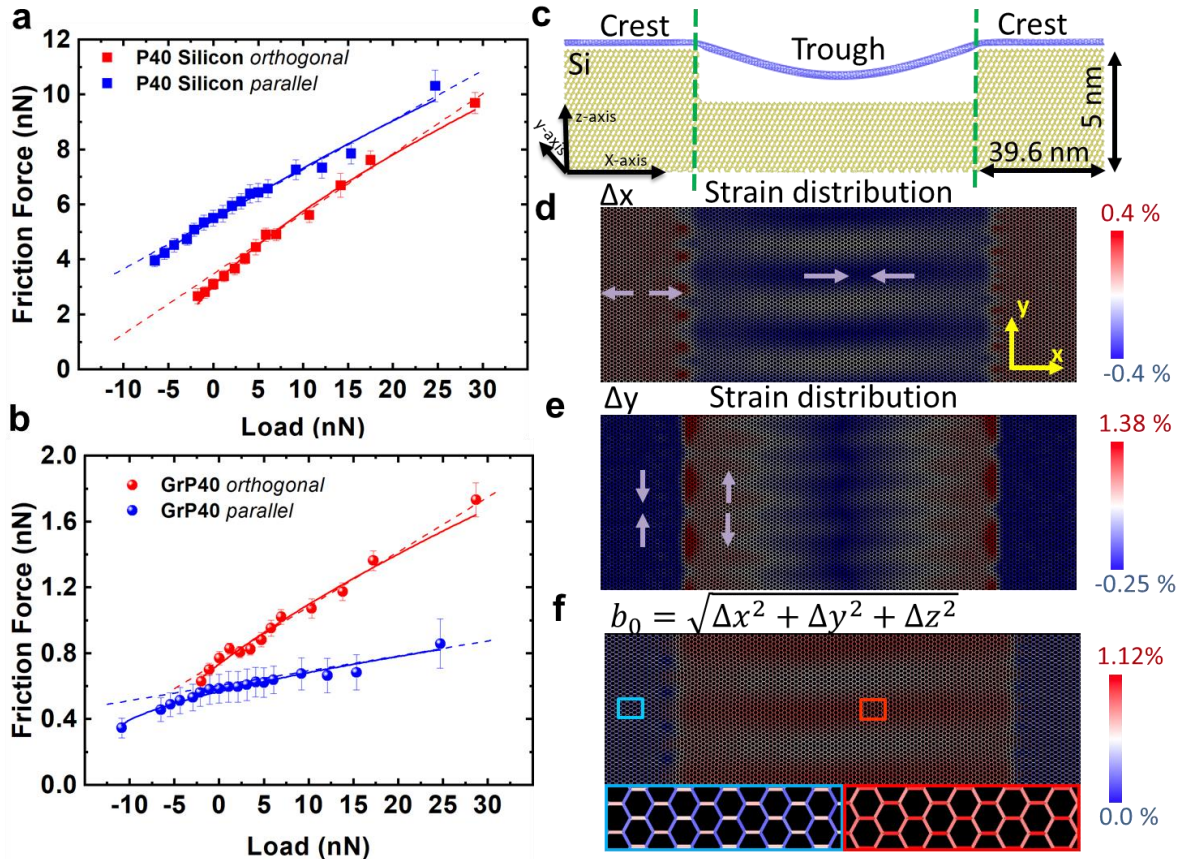
**Figure 4: Friction Force as a function of load applied to groove axis and strain distribution:** Experimental data of load dependent friction force curves on GrP40 sample with the grooves axis oriented parallel (blue) and perpendicular (red) to the fast scan direction; (a) on bare silicon textured surface (b) on adjacent graphene covered region. Square and circular shaped data represent the experimental values, continuous lines are the fitting curve from DMT model and dashed line is the linear fit. (c) MD simulation of a graphene sheet sags into the P40 textured Si surface. The vertical drawn dashed green lines represent the trough region of suspended graphene between two crests. (d) Strain distribution based on bond strain variation along the x-axis ($\Delta x$), (e) y-axis ($\Delta y$) and (f) total bond length ($b_0$). The Inset region (marked by the coloured rectangle in panel (f)) shows the variation in C-C bond length in the crest and trough regions. The asymmetry in $b_0$ between different regions and along different axes is readily apparent, as shown in the zoom-in image.

The anisotropic values of the friction force for the graphene covered textured surface can be explained through anisotropic stretching/compression of C-C bonds in orthogonal directions over an individual groove. It has been validated through MD simulation for graphene over P40 architecture, as shown

in **Figure 4 (c)**. The carbon-silicon interaction has been implemented using a Lennard Jones 6-12 potential with $\varepsilon$ (Si-C) = 8.909 meV and $\sigma$ (Si-C) = 0.3326 nm to model physisorption of the graphene monolayer on a silicon substrate[70,71]. The strain distribution in graphene over the crest and trough (between green dashed lines in panel (c)) in orthogonal (x), parallel (y) and out-of-plane to the silicon surface has been calculated through percentage changes in $\Delta x$, $\Delta y$ and bond length $b_o=$ $\sqrt{\Delta x^2 + \Delta y^2 + \Delta z^2}$ with respect to Gr/Flat (see Supplementary Information **S4** for details) respectively, and is shown in **Figure 4 (d, e, f)**. Along the x-axis, the carbon atoms of graphene at a crest are continually stretched until the crest-trough interface is reached (red colour). The localised stretching of C-C bonds at the interface leads to a net compressive strain distribution at the trough of equal magnitude, see scale bar at **Figure 4 (d)**. Along the y-axis, the crest region weakly compresses the C-C bond in contrast to the $\Delta x$ strain distribution, but a significant tensile strain dominates from interface to the trough region. Thus, there is a net tensile strain resulting from the combined effect of substrate adhesion and adjacent suspended graphene, see **Figure 4 (e)**.

The integral bond length ($b_o$) distribution at the crest illustrates asymmetric bond alteration along the orthogonal (stretching) and parallel (compressive) directions relative to the groove axis. This asymmetry is also sustained at the trough, but a higher magnitude observed (see **Figure 4(f))** and its inset marked by rectangles). Thus, the friction force is lowest whilst sliding perpendicular to the stretched axis of graphene. Also, this distinction in the bond length distribution results in anisotropy in friction forces orthogonal and parallel to the groove axis. It clearly shows the remarkable anisotropic tribological (friction force, COF, S) performance of graphene over the same textured surface, which is not possible for a traditional Gr/Flat system. Thus, graphene covered textured systems could bring an era of tuned friction force in nanoscale, which has been a non-trivial task in the last decades. Moreover, such regulated friction could enhance the performance of nanomachines.
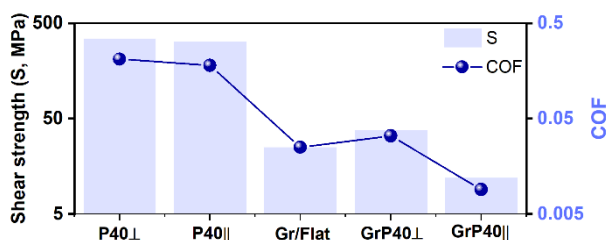


**Figure 5: Shear strength (MPa) and COF values of nanogear.** The modulation in the shear strength (S, MPa) and COF values at different scanning directions. Graphene on a flat surface lies intermediate values between scanning parallel ($\parallel$) and perpendicular ($\perp$) to the groove axis.

**Conclusion**

In summary, the deposition of graphene over textured silicon surfaces can offer a wide range of opportunities due to the interplay between adhesion force energy, bending, stretching, and strained orientation. By controlling the groove separation distance in the substrate, a tuneable strain in a single layer of graphene can be achieved, presented through the analytical modelling, MD simulation and Raman spectroscopic measurements. The graphene deposited over a flat Si surface undergoes compressive strain, which is released over the textured surfaces. The overlayered graphene also drops the friction force values at the extent of extreme lubricity and channelizes the friction dissipation while sliding, complementary to the textured geometry. The strain distribution in graphene over the textured architecture regulates the friction force; consequently, COF and S values. Thus, single-layer graphene deposited onto an anisotropic nanotextured system could acquire diverse nanomechanical properties. It is demonstrated in reference to the FFM that depends on the sliding direction with respect to grooves orientation. The presented work will pave the pathway to nanoscale devices for efficient functioning and controlled motion of nanoscale objects, particularly in nanomechanical devices and nanorobotics.

**Materials and Methods Section**

Deposition of graphene over textured surface: Commercially available single-layer CVD graphene from ACS Material (Pasadena, CA-USA) and Graphenea Inc. (Spain) were deposited on nanostructured surfaces through the standard method of polymer assisted wet transfer followed by removal of polymer residue in an acetone bath (40°C for 30 min). Later, samples were dried in the oven at 40°C for 20 min and sequentially heated in a vacuum at 300°C for 2 hrs. The validation of distribution of single graphene layer is carried out by Raman spectroscopy through an intensity ratio of 2D/G > 1.3. AFM assisted mechanical cleaning have been conducted by a sacrificial cantilever prior to the friction measurements.

Raman measurements: Raman Spectroscopy is carried out by using a Renishaw inVia confocal Raman microscope. The laser line used for the investigation was $\lambda$ = 532 nm (Source: Solid-state, model RL53250) and 1800 groove mm$^{-1}$ grating. All the measurements were performed at 10% laser power (controlled through ND filters) with 5 second exposure at 100X magnification. This set-up can provide the spectral resolution up to 0.3 cm$^{-1}$ and the penetration depth up to 0.7-0.93 µm for Si wafer[72], which is sufficient for our investigation. The Raman modes of G and 2D peaks are fitted with Lorentzian curve to evaluate the peak positions (cm$^{-1}$) and peak intensity.

Atomic force microscopy and Friction Force Microscopy: Two different Atomic Force Microscope (AFM) were utilized during the experiments. The Bruker Dimension Icon with Peak Force Tapping Mode$^{TM}$ option and the NT-MDT NTEGRA AURA system. All the measurements were carried out in

air, under ambient conditions. Commercially available rectangular shaped silicon cantilevers (MikroMaschHQ: CSC37/NoAl) with nominal normal elastic constants between 0.2 and 0.8 N m$^{-1}$ were used for Friction Force Microscopy (FFM) measurements. The detailed calibration procedure for the measurements is mentioned in supplementary **S5**.

**Acknowledgement:**

**References**

(1)   Balčytis, A.; Juodkazytė, J.; Seniutinas, G.; Li, X.; Niaura, G.; Juodkazis, S. In *Laser-based Micro- and Nanoprocessing X*; Klotzbach, U., Washio, K., Arnold, C. B., Eds.; 2016; Vol. 9736, p 97360G.

(2)   Zang, X.; Zhou, Q.; Chang, J.; Liu, Y.; Lin, L. *Microelectron. Eng.* **2015**, *132*, 192–206.

(3)   Bico, J.; Thiele, U.; Quéré, D. *Colloids Surfaces A Physicochem. Eng. Asp.* **2002**, *206* (1-3), 41–46.

(4)   Cottin-Bizonne, C.; Barrat, J.-L.; Bocquet, L.; Charlaix, E. *Nat. Mater.* **2003**, *2* (4), 237–240.

(5)   Dobrzański, L. A.; Drygała, A.; Gołombek, K.; Panek, P.; Bielańska, E.; Zieba, P. *J. Mater. Process. Technol.* **2008**, *201* (1-3), 291–296.

(6)   Hemker, K. J.; Sharpe Jr, W. N. *Annu. Rev. Mater. Res.* **2007**, *37*, 93–126.

(7)   Finkbeiner, S. In *2013 Proceedings of the ESSCIRC (ESSCIRC)*; IEEE, 2013; pp 9–14.

(8)   Mukherjee, S.; Aluru, N. R. Applications in micro-and nanoelectromechanical systems, 2006.

(9)   Hu, Y.-Z.; Ma, T.-B. In *Comprehensive Nanoscience and Technology*; Elsevier, 2011; Vol. 1-5, pp 383–418.

(10)  Xue, Y.; Shi, X.; Huang, Q.; Zhang, K.; Wu, C. *Tribol. Int.* **2021**, *161* (May), 107099.

(11)  Rapoport, L.; Moshkovich, A.; Perfilyev, V.; Lapsker, I.; Halperin, G.; Itovich, Y.; Etsion, I. *Surf. Coatings Technol.* **2008**, *202* (14), 3332–3340.

(12) Ping, Y.; Bo, L. N.; Daoguo, Y.; Ernst, L. J. *Microsyst. Technol.* **2006**, *12* (12), 1125–1131.

(13) Tripathi, M.; Awaja, F.; Bizao, R. A.; Signetti, S.; Iacob, E.; Paolicelli, G.; Valeri, S.; Dalton, A.; Pugno, N. M. *ACS Appl. Mater. Interfaces* **2018**, *10* (51), 44614–44623.

(14) Klein, J.; Kumacheva, E. *Science (80-. ).* **1995**, *269* (5225), 816–819.

(15) Fajardo, O. Y.; Bresme, F.; Kornyshev, A. A.; Urbakh, M. *Sci. Rep.* **2015**, *5*, 7698.

(16) Al-Azizi, A. A.; Eryilmaz, O.; Erdemir, A.; Kim, S. H. *Langmuir* **2013**, *29* (44), 13419–13426.

(17) Lee, S.; Spencer, N. D. *Science (80-. ).* **2008**, *319* (5863), 575–576.

(18) Hod, O.; Meyer, E.; Zheng, Q.; Urbakh, M. *Nature* **2018**, *563* (7732), 485–492.

(19) Rosenkranz, A.; Costa, H. L.; Baykara, M. Z.; Martini, A. *Tribol. Int.* **2021**, *155* (October 2020), 106792.

(20) Mutyala, K. C.; Wu, Y. a.; Erdemir, A.; Sumant, A. V. *Carbon N. Y.* **2019**, *146*, 524–527.

(21) Wang, C.; Li, H.; Zhang, Y.; Sun, Q.; Jia, Y. *Tribol. Int.* **2014**, *77*, 211–217.

(22) Wyatt, B. C.; Rosenkranz, A.; Anasori, B. *Adv. Mater.* **2021**, *33* (17), 2007973.

(23) Malaki, M.; Varma, R. S. *Adv. Mater.* **2020**, *32* (38), 1–20.

(24) Rodriguez, A.; Jaman, M. S.; Acikgoz, O.; Wang, B.; Yu, J.; Grützmacher, P. G.; Rosenkranz, A.; Baykara, M. Z. *Appl. Surf. Sci.* **2021**, *535* (May 2020), 147664.

(25) Lavini, F.; Calò, A.; Gao, Y.; Albisetti, E.; Li, T.-D.; Cao, T.; Li, G.; Cao, L.; Aruta, C.; Riedo, E. *Nanoscale* **2018**, *10* (17), 8304–8312.

(26) Yong, K.; Ashraf, A.; Kang, P.; Nam, S. *Sci. Rep.* **2016**, *6* (1), 24890.

(27) Zhang, D.-B.; Akatyeva, E.; Dumitrică, T. *Phys. Rev. Lett.* **2011**, *106* (25), 255503.

(28) Chen, H.; Chen, S. *J. Phys. D. Appl. Phys.* **2013**, *46* (43), 435305.

(29) Vazirisereshk, M. R.; Ye, H.; Ye, Z.; Otero-de-la-Roza, A.; Zhao, M.-Q.; Gao, Z.; Johnson, A. T. C.; Johnson, E. R.; Carpick, R. W.; Martini, A. *Nano Lett.* **2019**, *19* (8), 5496–5505.

(30) Chilkoor, G.; Shrestha, N.; Kutana, A.; Tripathi, M.; Robles Hernández, F. C.; Yakobson, B. I.; Meyyappan, M.; Dalton, A. B.; Ajayan, P. M.; Rahman, M. M.; Gadhamshetty, V. *ACS Nano* **2021**, 3987.

(31) Paolicelli, G.; Tripathi, M.; Corradini, V.; Candini, a.; Valeri, S. *Nanotechnology* **2015**, *26* (5).

(32) Tripathi, M.; Lee, F.; Michail, A.; Anestopoulos, D.; McHugh, J. G.; Ogilvie, S. P.; Large, M. J.; Graf, A. A.; Lynch, P. J.; Parthenios, J.; Papagelis, K.; Roy, S.; Saadi, M. A. S. R.;

Rahman, M. M.; Pugno, N. M.; King, A. A. K.; Ajayan, P. M.; Dalton, A. B. *ACS Nano* **2021**, *15* (2), 2520–2531.

(33)    Zande, A. M. van der; Barton, R. A.; Alden, J. S.; Ruiz-Vargas, C. S.; Whitney, W. S.; Pham, P. H. Q.; Park, J.; Parpia, J. M.; Craighead, H. G.; McEuen, P. L. *Nano Lett.* **2010**, *10* (12), 4869–4873.

(34)    Levy, N.; Burke, S. A.; Meaker, K. L.; Panlasigui, M.; Zettl, A.; Guinea, F.; Neto, A. H. C.; Crommie, M. F. *Science (80-. ).* **2010**, *329* (5991), 544–547.

(35)    Wagner, T. J. W.; Vella, D. *Appl. Phys. Lett.* **2012**, *100* (23).

(36)    Wang, X.; Tantiwanichapan, K.; Christopher, J. W.; Paiella, R.; Swan, A. K. *Nano Lett.* **2015**, *15* (9), 5969–5975.

(37)    Wang, C.; Chen, S. *Sci. Rep.* **2015**, *5*, 1–6.

(38)    Dai, C.; Guo, Z.; Zhang, H.; Chang, T. *Nanoscale* **2016**, *8* (30), 14406–14410.

(39)    Kwon, S.; Ko, J.-H.; Jeon, K.-J.; Kim, Y.-H.; Park, J. Y. *Nano Lett.* **2012**, *12* (12), 6043–6048.

(40)    Ko, J.-H.; Kwon, S.; Byun, I.-S.; Choi, J. S.; Park, B. H.; Kim, Y.-H.; Park, J. Y. *Tribol. Lett.* **2013**, *50* (2), 137–144.

(41)    Lee, C.; Li, Q.; Kalb, W.; Liu, X. Z.; Berger, H.; Carpick, R. W.; Hone, J. *Science (80-. ).* **2010**, *328* (5974), 76–80.

(42)    Paolicelli, G.; Tripathi, M.; Corradini, V.; Candini, A.; Valeri, S. *Nanotechnology* **2015**, *26* (5), 055703.

(43)    Zhang, S.; Hou, Y.; Li, S.; Liu, L.; Zhang, Z.; Feng, X.-Q.; Li, Q. *Proc. Natl. Acad. Sci.* **2019**, *116* (49), 24452–24456.

(44)    Rota, A.; Tripathi, M.; Gazzadi, G.; Valeri, S. *Langmuir* **2013**, *29* (17), 5286–5293.

(45)    Dell'Anna, R.; Iacob, E.; Tripathi, M.; Dalton, A.; Böttger, R.; Pepponi, G. *J. Microsc.* **2020**, No. 1, jmi.12908.

(46)    Pirkle, A.; Chan, J.; Venugopal, A.; Hinojos, D.; Magnuson, C. W.; McDonnell, S.; Colombo, L.; Vogel, E. M.; Ruoff, R. S.; Wallace, R. M. *Appl. Phys. Lett.* **2011**, *99* (12), 2009–2012.

(47)    Bunch, J. S.; Dunn, M. L. *Solid State Commun.* **2012**, *152* (15), 1359–1364.

(48)    Cullen, W. G.; Yamamoto, M.; Burson, K. M.; Chen, J.-H.; Jang, C.; Li, L.; Fuhrer, M. S.; Williams, E. D. *Phys. Rev. Lett.* **2010**, *105* (21), 215504.

(49)    Zhang, Y.; Heiranian, M.; Janicek, B.; Budrikis, Z.; Zapperi, S.; Huang, P. Y.; Johnson, H. T.; Aluru, N. R.; Lyding, J. W.; Mason, N. *Nano Lett.* **2018**, *18* (3), 2098–2104.

466    (50)   Lazzeri, M.; Mauri, F. *Phys. Rev. Lett.* **2006**, *97* (26), 266407.

467    (51)   Goniszewski, S.; Adabi, M.; Shaforost, O.; Hanham, S. M.; Hao, L.; Klein, N. *Sci. Rep.*
468          **2016**, *6* (1), 22858.

469    (52)   Kong, C.; Pilger, C.; Hachmeister, H.; Wei, X.; Cheung, T. H.; Lai, C. S. W.; Lee, N. P.;
470          Tsia, K. K.; Wong, K. K. Y.; Huser, T. *Light Sci. Appl.* **2020**, *9* (1).

471    (53)   Hinnefeld, J. H.; Gill, S. T.; Mason, N. *Appl. Phys. Lett.* **2018**, *112* (17), 173504.

472    (54)   Lee, J. E.; Ahn, G.; Shim, J.; Lee, Y. S.; Ryu, S. *Nat. Commun.* **2012**, *3*, 1024.

473    (55)   Balois, M. V.; Hayazawa, N.; Yasuda, S.; Ikeda, K.; Yang, B.; Kazuma, E.; Yokota, Y.; Kim,
474          Y.; Tanaka, T. *npj 2D Mater. Appl.* **2019**, *3* (1), 38.

475    (56)   Lee, J. K.; Yamazaki, S.; Yun, H.; Park, J.; Kennedy, G. P.; Kim, G. T.; Pietzsch, O.;
476          Wiesendanger, R.; Lee, S.; Hong, S.; Dettlaff-Weglikowska, U.; Roth, S. *Nano Lett.* **2013**, *13*
477          (8), 3494–3500.

478    (57)   Gnecco, E.; Pawlak, R.; Kisiel, M.; Glatzel, T.; Meyer, E. In *Nanotribology and*
479          *Nanomechanics*; Springer International Publishing: Cham, 2017; pp 519–548.

480    (58)   Zhang, S.; Ma, T.; Erdemir, A.; Li, Q. *Mater. Today* **2019**, *26* (June), 67–86.

481    (59)   Deng, Z.; Klimov, N. N.; Solares, S. D.; Li, T.; Xu, H.; Cannara, R. J. *Langmuir* **2013**, *29*
482          (1), 235–243.

483    (60)   Manini, N.; Mistura, G.; Paolicelli, G.; Tosatti, E.; Vanossi, A. *Adv. Phys. X* **2017**, *2* (3),
484          569–590.

485    (61)   Gallagher, P.; Lee, M.; Amet, F.; Maksymovych, P.; Wang, J.; Wang, S.; Lu, X.; Zhang, G.;
486          Watanabe, K.; Taniguchi, T.; Goldhaber-Gordon, D. *Nat. Commun.* **2016**, *7* (1), 10745.

487    (62)   Berardo, A.; Costagliola, G.; Ghio, S.; Boscardin, M.; Bosia, F.; Pugno, N. M. *Mater. Des.*
488          **2019**, *181*, 107930.

489    (63)   Almeida, C. M.; Prioli, R.; Fragneaud, B.; Cançado, L. G.; Paupitz, R.; Galvão, D. S.; De
490          Cicco, M.; Menezes, M. G.; Achete, C. A.; Capaz, R. B. *Sci. Rep.* **2016**, *6* (June), 1–9.

491    (64)   Choi, J. S.; Kim, J.-S.; Byun, I.-S.; Lee, D. H.; Lee, M. J.; Park, B. H.; Lee, C.; Yoon, D.;
492          Cheong, H.; Lee, K. H.; Son, Y.-W.; Park, J. Y.; Salmeron, M. *Science (80-. ).* **2011**, *333*
493          (6042), 607–610.

494    (65)   Carpick, R. W.; Ogletree, D. F.; Salmeron, M. *Area* **1999**, *400*, 395–400.

495    (66)   Schwarz, U. D.; Zwörner, O.; Köster, P.; Wiesendanger, R. *Phys. Rev. B - Condens. Matter*
496          *Mater. Phys.* **1997**, *56* (11), 6997–7000.

497    (67)   Jacobs, T. D. B.; Martini, A. *Appl. Mech. Rev.* **2017**, *69* (6).

(68)     Lang, H.; Peng, Y.; Cao, X.; Zou, K. *ACS Appl. Mater. Interfaces* **2020**, *12* (22), 25503–25511.

(69)     Buzio, R.; Gerbi, A.; Uttiya, S.; Bernini, C.; Del Rio Castillo, A. E.; Palazon, F.; Siri, A. S.; Pellegrini, V.; Pellegrino, L.; Bonaccorso, F. *Nanoscale* **2017**, *9* (22), 7612–7624.

(70)     Kaftory, M.; Kapon, M.; Botoshansky, M. In *Wiley, Chichester*; 1998; Vol. 121, pp 181–265.

(71)     Los, J. H.; Fasolino, A. *Phys. Rev. B* **2003**, *68* (2), 024107.

(72)     Xu, Z.; He, Z.; Song, Y.; Fu, X.; Rommel, M.; Luo, X.; Hartmaier, A.; Zhang, J.; Fang, F. *Micromachines* **2018**, *9* (7), 361.